Surface Chemistry of Ternary Nanocrystals: Engineering the Deposition of Conductive $NaBiS_2$ Films

Alan M. Medina-Gonzalez,[1] Bryan A. Rosales,[1,†] Umar H. Hamdeh,[2] Matthew G. Panthani,[2] Javier Vela*,[1,3]

[1]Department of Chemistry Iowa State University, [2]Department of Chemical and Biological Engineering, Iowa State University, and [3]Ames Laboratory, Iowa State University, Ames, Iowa 50011, United Sates.

ABSTRACT: The ability to engineer the surface chemistry of complex ternary nanocrystals is critical to their successful application in photovoltaic, thermoelectric, and other energy conversion devices. For many years, several studies have shed light into the surface chemistry of unary and binary semiconductor nanocrystals, as well as their surface modification with monodentate and multidentate ligands in a variety of applications. In contrast, our understanding of the surface chemistry and ligand modification of ternary and other complex multinary nanocrystals remains relatively limited. Recently, our group reported the synthesis of colloidal $NaBiS_2$ semiconductor nanocrystals with sizes tunable between 2–60 nm, and a light absorption edge of *ca.* 1.4 eV. Here, we use a combination of infrared and nuclear magnetic resonance spectroscopies to show that the as-made $NaBiS_2$ nanocrystals are capped by oleylamine and neodecanoate ligands. We investigate biphasic liquid-liquid exchange as a means to replace these native ligands with either carboxylate-terminated lipoic acid or with small iodide ligands, leading in both cases to solubility in polar solvents—such as methanol, water, and dimethylformamide. We also investigate a layer-by-layer, biphasic solid-liquid exchange approach to prepare films of $NaBiS_2$ nanocrystals capped with halide ligands—iodide, bromide, chloride. Upon exchange and removal of the native ligands, we show that the resistance of $NaBiS_2$ nanocrystal films greatly decreases, with their measured conductivity being comparable to that of films made of isostructural PbS nanocrystals, which have been used in solar cells. Lastly, we report the first solar cell device made of $NaBiS_2$ nanocrystal films with a limited power conversion efficiency (PCE) of 0.07. Further nanostructuring and ligand optimization may enable the preparation of much more efficient energy conversion devices based on $NaBiS_2$ as well as other non-toxic and Earth-abundant, biocompatible multinary semiconductors.

Introduction

Ternary $APnE_2$ compounds (A = Li^+, Na^+, K^+, Rb^+, Cs^+, Cu^+, Ag^+, Tl^+; Pn = As^{3+}, Sb^{3+}, Bi^{3+}; E = S^{2-}, Se^{2-}, Te^{2-}) are a family of 72 semiconducting materials with band gaps ranging from 0.1–1.5 eV. These compounds have recently attracted considerable attention due to their potential applications in solar cells,[1,2,3] thermoelectrics,[4,5] photodetectors,[6,7] and batteries.[8] As an example, given their relatively biocompatible composition, 1.4 eV band gap, and high extinction coefficients of 10^4–10^5 cm^{-1} M^{-1}, $NaBiS_2$ nanocrystals could be excellent building blocks for energy conversion devices.[9]

Normally, the use of nanocrystals in optoelectronic devices requires the ability to exchange insulating long-chain organic ligands for much smaller inorganic ligands, so that charge carriers can be more efficiently transported across nanocrystal films.[10] In general, in terms of what native ligands are originally present on their surface, as well as how ligand exchange affects their properties, the surface chemistry of unary semiconductor nanocrystals is somewhat well established. For example, Si nanocrystals undergo silicide oxidation, halide reduction, and hydrazination, which can result in improved photoluminescence quantum yields.[11] Solid state (ss) NMR shows that the precise speciation and relative population of mono-, bi-, and tri-hydride species on the surface of Si nanocrystals.[12] In turn, the photovoltage of Ge nanocrystals is known to be affected by exchanging the native oleylamine (oleylNH_2) ligands with dodecanethiol (DDT).[13] The native ligands on Ge nanocrystals synthesized in a gas-phase plasma reactor can be exchanged with a variety of short inorganic ligands to produce an electroactive layer.[14]

Even more so than unary nanocrystals, the surface chemistry and ligand exchange behavior of binary semiconductor nanocrystals (II-VI, III-V, etc.) are well established. One of the first modern studies in this area was the exchange of pyridine onto CdSe nanocrystals that were originally capped with tri-n-octylphosphine (TOP), which was characterized by NMR.[15] Several binary systems with various morphologies undergo ligand exchange with small metal chalcogenide complexes in different solvents.[16] For example, PbS quantum dots retain colloidal stability—*i.e.*, remain soluble and stable—in a polar solvent, while also retaining photoluminescence stability; these quantum dots can be subsequently used in the preparation of highly conductive films.[17] In addition, various monodentate and bidentate head groups affect the conduction and valence band energy levels of PbS quantum dots.[18,19,20] In the case of Zn_3P_2 nanocrystals, the native methyl ligands can be exchanged for longer chain ligands in order to enhance homogenous dispersion in solution.[21] In the case of Bi_2S_3, the native ligands can be removed and exchanged for various ligands.[22,23,24,25]

Films of Bi_2S_3 nanocrystals capped with ethanedithiol[26] (EDT) or hydrazine[27] show conductive behavior with values in the range of ~10^{-6}–10^{-5} S cm^{-1}.

In contrast to all that is known about unary and binary nanocrystals, we know relatively little about the surface chemistry and ligand exchange behavior of multinary colloidal nanocrystals. $CuInE_2$ or "CIS" nanocrystals (E = S or Se) can be capped with various organic and inorganic ligands in order to improve photoluminescence quantum yields and enhance their performance in solar cells.[28,29,30,31] Similarly, Cu_2ZnSnE_4 or "CZTS" and Cu-III-Se_2 or "CIGS" nanocrystals (E = S, Se, and III = Ga or In) undergo solution phase exchange with various capping ligands, enabling the fabrication of thin films for solar cells.[32,33,34] Various thiolate and amine complexes are known to coordinate to the surface of $AgSbS_2$ nanocrystals.[35] In turn, $CsPbX_3$ (X = Cl, Br, I) nanocrystals display highly dynamic coordination chemistry,[36,37] and their native surface can be exchanged with various cationic and anionic ligands.[38,39,40,41]

$NaBiE_2$ nanocrystals (E = S or Se) adopt a ternary rock salt structure in which mixed Na^+/Bi^{3+} cation sites are stuffed into the octahedral holes of an fcc arrangement of chalcogenide (E^{2-}) ions. $NaBiS_2$ can be thought of as isostructural to PbS, with mixed Na^+/Bi^{3+} sites replacing Pb^{2+}. Such rock salt nanocrystals are known to exhibit cationic (111) and mixed cation-anion (100) surface planes.[42,43,44] Previously, we reported similarities in the surface chemistry between binary and ternary rock salt compounds.[9] Calculations performed on related $AgBiS_2$ nanocrystals suggest these may prefer having a Ag-rich surface.[45]

In this work, we study the fundamental surface chemistry of these ternary rock salt colloidal $NaBiS_2$ nanocrystals. We show that the surface of the as-made nanocrystals is terminated with oleylamine and neodecanoate ligands. We develop a facile liquid-liquid biphasic ligand exchange method to produce $NaBiS_2$ nanocrystals soluble in polar solvents by capping them with lipoic acid and alkali metal halides. Lastly, we successfully fabricate conducting $NaBiS_2$ films *via* a solid-liquid ligand exchange using a layer-by-layer (LbL) approach, and demonstrate the use of $NaBiS_2$ films as the active layer in solar cell devices. Further improvements in nanocrystal passivation and charge separation in their films will enhance the potential of $NaBiS_2$ nanocrystals for photovoltaics, thermoelectric, and other energy conversion devices.

Results and Discussion

Colloidally stable $NaBiS_2$ nanocrystals. $NaBiS_2$ nanocrystals with an absorption onset of 1.40 eV can be conveniently prepared from the solution phase reaction between commercially available metal carboxylates (sodium oleate and bismuth neodecanoate) and elemental sulfur in oleylamine (Scheme 1 and Figure 1, see Experimental).[9] By varying the reaction (growth) temperature, this approach produces highly spherical and monodisperse nanocrystals with sizes tunable between 2.6–21 nm (see Supporting Information or S.I.). We note that this synthesis exhibits a critical ripening temperature of 230 °C, at and above which colloidal stability decreases. Below this temperature, nanocrystal sizes vary between 2.6–6.7 nm, with small standard deviations of < 0.6 nm, based on the Scherrer equation. In contrast, temperatures between 230–250 °C cause significant ripening, with sizes varying between 6.7–21 nm and standard deviations increasing to 2 nm.

Scheme 1.

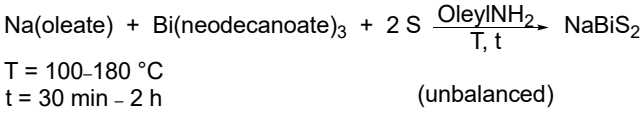

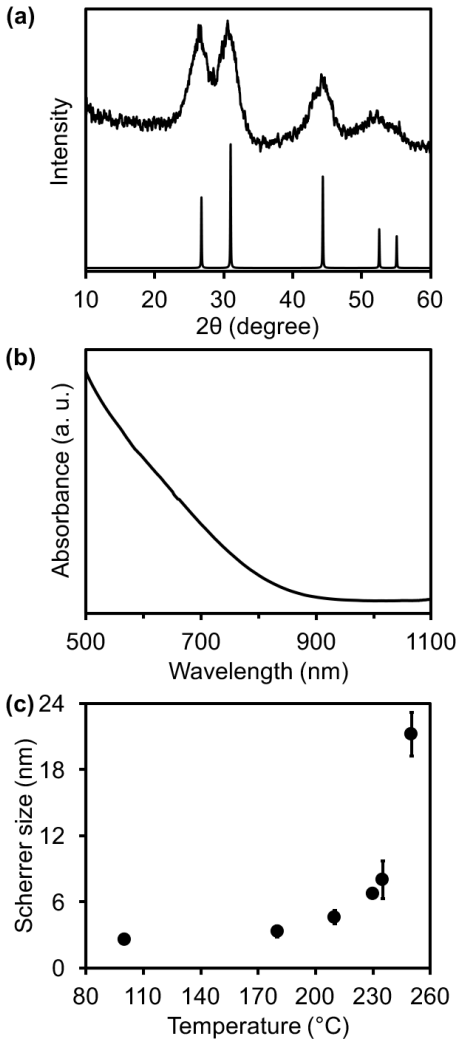

Figure 1. (a) Experimental *vs.* standard powder XRD, and (b) solution-phase absorption spectrum of 2.9±0.6 nm $NaBiS_2$ nanocrystals prepared at 100 °C for 2 h. (c) Dependence of $NaBiS_2$ nanocrystal size on reaction (growth) temperature held for 2 h.

Coordination chemistry: What is on the surface? Several ligands (X-, L-, Z-type) are known to coordinate to the surface of II-VI binary semiconductor nanocrystals. According to Owen's adaptation of Green's ligand classification (Figure 2),[46,47] X-type ligands are negatively charged two-electron donors (*i.e.*, anionic Lewis bases), L-type ligands are neutral two-electron donors (*i.e.*, neutral Lewis bases), and Z-type

ligands are electronically unsaturated two-electron acceptors (*i.e.*, Lewis acids). Because of the increasing complexity of ternary systems, one could expect that a mixture of L-, Z-, and X-type ligands will bind to the surface of $NaBiS_2$ nanocrystals. Among these, there are X- (carboxylates) and Z-type (Na- and Bi-based Lewis acids) ligands that originate from either or both of the metal carboxylate precursors used during synthesis. Also, L-type ligands (thioamides and related compounds), which are produced from the reaction between elemental sulfur and oleylamine may be present (Figure 2).[48]

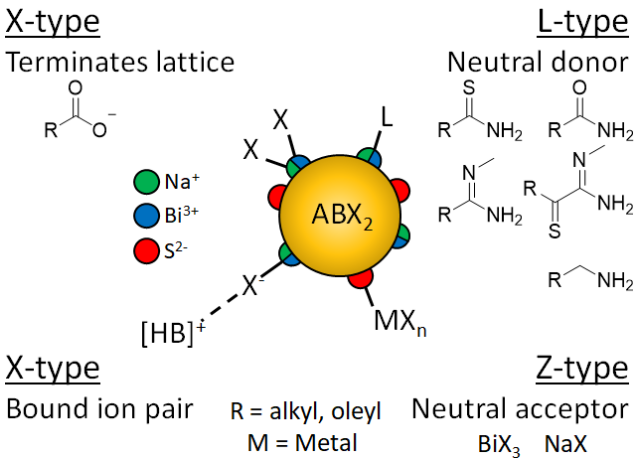

Figure 2. Classification of various types of ligands on the surface of $NaBiS_2$ nanocrystals based on the Green-Owen nomenclature.[46,47] Note: Based on IR data, carboxylate (X-type) ligands bind in a chelating (bidentate or η^2) fashion (see below).[49]

To test the presence of different ligands on the nanocrystal surface, we resorted to infrared (IR) and ^{1}H NMR spectroscopy. The IR of as made $NaBiS_2$ nanocrystals shows characteristic carboxylate vibrational modes (Figure 3a). The absence of a broad band between 2500–3300 cm^{-1}—ν(COO-H) as well as the small difference (Δ) between the asymmetric and symmetric stretching frequencies located between 1500–1600 cm^{-1}—$\nu_{as}(COO^-) - \nu_s(COO^-)$, under < 200 cm^{-1}—confirm that surface carboxylates are deprotonated. The exact value of Δ is strongly indicative of the type of carboxylate binding (see Figure 4, and Supporting Information or SI).[49,50,51] Large Δ values such as those observed for the free protonated carboxylic acids (≈ 250–300 cm^{-1}) are consistent with monodentate or η^1-binding—*i.e.*, coordination through a single oxygen; whereas small Δ values such as those observed for sodium oleate (120 cm^{-1}), bismuth neodecanoate (68 cm^{-1}), and the carboxylates on the $NaBiS_2$ nanocrystal surface (93 cm^{-1}) are consistent with bidentate or η^2-binding—coordination through both oxygens.[50]

IR also shows vibrational modes characteristic of amines (Figure 3b). Specifically, a $\nu(NH_2)$ stretch at ~3300 cm^{-1}, and a (N-H) bending shoulder at ~1600 cm^{-1}, as well as another ν(C-N) stretch at ~1100 cm^{-1} are consistent with surface oleylamine. In contrast to what is observed for free oleylamine, the asymmetric and symmetric stretches ($\nu_{as}(NH_2)$ and $\nu_s(NH_2)$, respectively) on the nanocrystal surface appear as a single band. The presence of a single $\nu_s(NH_2)$ stretch and the absence of a second $\nu_{as}(NH_2)$ stretch peaks usually indicates that oleylamine is hydrogen bonded to nearby anions, such as perhaps S^{2-} or COO^- on the nanocrystal surface.[52] Thus, IR strongly suggests that the surface of as made $NaBiS_2$ nanocrystals is coordinated by a mixture of chelating carboxylates (see below) as well as oleylamine ligands.

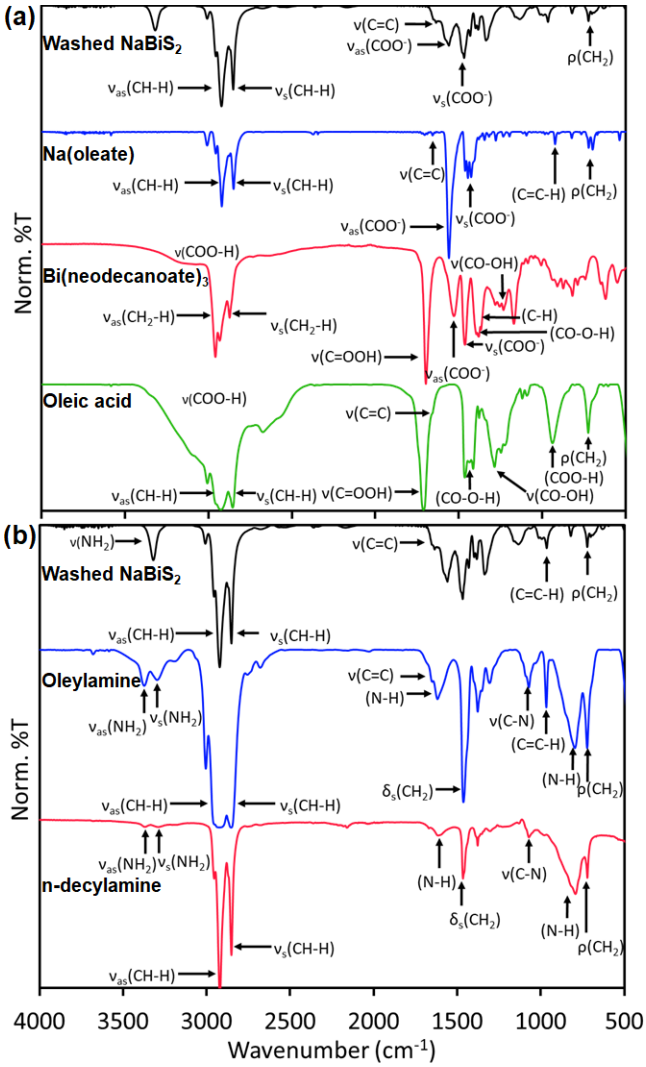

Figure 3. Infrared (IR) spectra of as made $NaBiS_2$ nanocrystals and relevant carboxylates (a) and amines (b). The differences (Δ) between asymmetric and symmetric stretches ($\nu_{as}(COO^-) - \nu_s(COO^-)$ in (a) are: $NaBiS_2$ nanocrystals (93 cm^{-1}, sodium oleate (120 cm^{-1}), bismuth neodecanoate (68 cm^{-1}), and oleic acid (254 cm^{-1}).

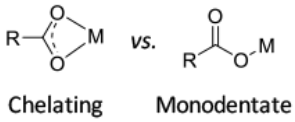

Figure 4. Chelating (bidentate or η^2-binding) *vs.* monodentate (η^1-binding) coordination (M = free or surface-bound Lewis acid).

The ^{1}H NMR of washed $NaBiS_2$ nanocrystals shows the typical broadening of surface-bound ligand resonances,

particularly for α- and β-methylene (-CH_2-) protons that are in very close proximity to the amine and carboxylate headgroups (see SI).[48,53] Critically, while $NaBiS_2$ nanocrystals consistently display a strong ^1H resonance for α-methylene protons bound to oleylamine (~2.6 ppm), they seem to lack any detectable peak for α-methylene protons bound to oleate (~2.4 ppm). Because $NaBiS_2$ nanocrystals show a very strong set of signals corresponding to chelating carboxylates by IR, and because they also show a very intense terminal methyl ^1H resonance by NMR—more so than would be expected from the olefinic and α-methylene integrations for oleylamine alone—we conclude that the surface of the $NaBiS_2$ nanocrystals also contains, in addition to oleylamine, neodecanoate ligands (but NOT oleate). Unlike oleate, which is a linear carboxylate, the neodecanoates used here are branched carboxylates that do not contain α-methylene protons (see SI). Based on its integration relative to that of the olefinic (-C<u>H</u>=C<u>H</u>-) and α-methylene (-C<u>H_2</u>NH_2) resonances from oleylamine, we find that about ~80% of the terminal aliphatic methyl resonance (-C<u>H_3</u>) originates from oleylamine, while ~20% comes from neodecanoates. However, because neodecanoate is introduced as mixture of multiple isomers, each with a different number of methyl groups per headgroup, we are unable to exactly determine the molar ratio of amine to carboxylate ligands at this time (see SI and Experimental).

Interestingly, the last observation above has significant mechanistic implications: During synthetic development of colloidal multinary semiconductors,[9,54,55,56,57] we and others have observed that the evolution of these complex phases is a stepwise, sequential process, where metallic and/or binary seeds often precede and, sometimes compete with, the formation of higher order multinary nanocrystals. In the particular case of $NaBiS_2$, we have reported that unary Bi^0—and then binary Bi_2S_3—seeds precede ternary evolution.[9] The fact that neodecanoate, originally bound to the bismuth precursor, is retained throughout this process, and found in the final nanocrystals, is consistent with this idea (Scheme 1). In contrast, oleate, originally bound to sodium, is lost and absent in the final nanocrystals, indicating that the sodium precursor may persist in solution for longer, until it is finally incorporated into the unary and/or binary seeds, in order to yield the final ternary phase.

Further confirmation that these ligands are bound to the surface comes from Diffusion Ordered NMR Spectroscopy (DOSY) (Figure 5).[49,53] DOSY is a pulsed field gradient NMR technique that is useful in spectroscopically resolving different compounds based on their size. In a DOSY experiment, multiple spin echo spectra are measured for varying pulsed field gradient strength, duration, or delays in the pulse sequence. Plots of the echo intensity as a function of the pulse field gradient strength or duration, then allow the self-diffusion coefficient (D) to be determined for individual peaks in the NMR spectrum. In practice, this means that that free, quickly diffusing molecules such as residual solvents ($CHCl_3$, EtOH) can be distinguished from surface-passivating ligands bound to much larger nanocrystals, based on the value of D. The diffusion coefficient of peaks corresponding to oleylamine and carboxylates (≈5 x 10^{-6} cm^2 s^{-1}) is significantly smaller than the residual purification solvent and residual protonated solvent peaks (≈1–2 x 10^{-5} cm^2 s^{-1}), strongly suggesting these ligands are part of the much larger nanocrystal compact. The hydrodynamic size calculated using the Stokes-Einstein equation (d_H = 1.6±0.5 nm) compares relatively well to that obtained by the Scherrer equation (2.1±1.7 nm).

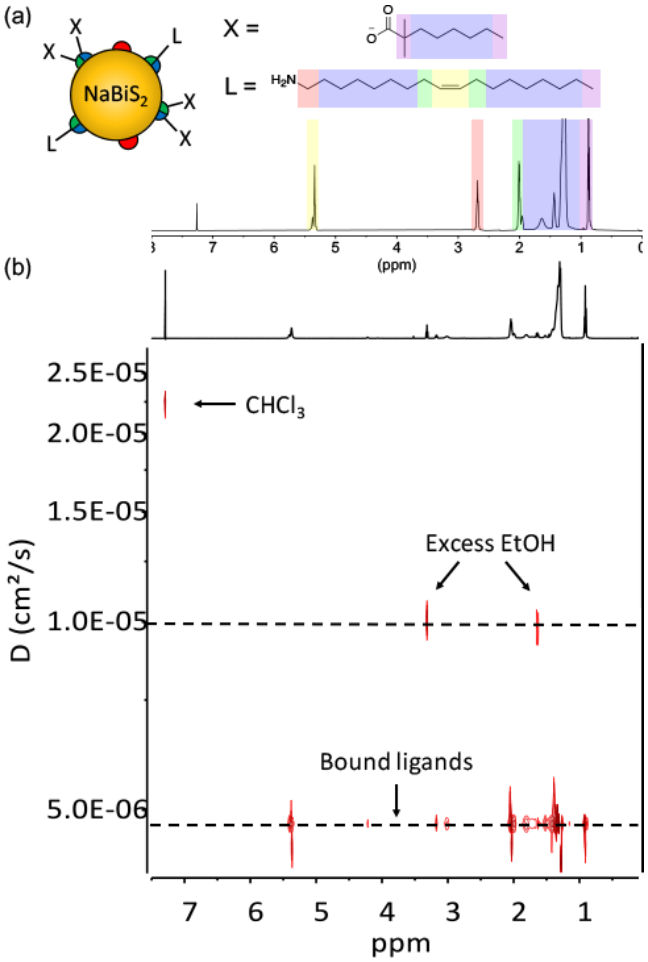

Figure 5. 1D ^1H NMR of 4.5±0.5 nm colloidal $NaBiS_2$ nanocrystals in $CDCl_3$ (a). 2D DOSY NMR of 2.1±1.7 nm colloidal $NaBiS_2$ nanocrystals in $CDCl_3$ (b); increasing (faster) diffusion coefficients (D) correspond to smaller, more freely diffusing species in solution.

Liquid-liquid biphasic ligand exchange. Colloidal nanocrystals undergo various types of ligand exchange reactions such as L-promoted Z-type displacement, which results in exchange of labile metal carboxylates by strong binding primary amines, phosphines, and multidentate ligands.[58] A common benefit of ligand exchange is that new capping ligands can affect and improve the optoelectronic properties of nanocrystals.[59,60] For example, more strongly passivating ligands can enhance the photoluminescence quantum yield of CdSe nanocrystals,[61] while ligands with different electron-donating abilities can shift the energies of the valence and conduction bands as well as alter the n- and p-type character of PbS nanocrystals.[62] Surface ligands can also be chemically modified to incorporate various functional groups before—without displacing the native ligands—or after ligand exchange.[49] Ternary lead halide perovskite nanocrystals exhibit highly dynamic ligands, and yet their

exact nature can impact their optical and structural properties as well as colloidal stability.[37,40,63]

The synthesis of highly luminescent binary quantum dots was initially developed using hydrophobic capping ligands (TOP/TOPO, oleylamine, oleate).[64] Light-promoted biphasic liquid-liquid conditions are now the method of choice to quickly exchange these non-polar native ligands with soft bidentate thiols.[65] In general, regardless of whether photochemical or thermal conditions are used, the use of carboxylate- or ammonium terminated thiols causes the binary colloidal nanocrystals to transfer from a nonpolar layer (hexane, chloroform, or toluene) into a more polar one (*e.g.*, methanol or water). In addition, CdSe nanocrystals can be capped with carboxylate-terminated tridentate thiolate ligands, enabling the production more robust aqueous photocatalysts for H_2 generation.[66,67,68]

Scheme 2. Ligand exchange in $NaBiS_2$ nanocrystals (X and X' ligands have a similar negative charge).

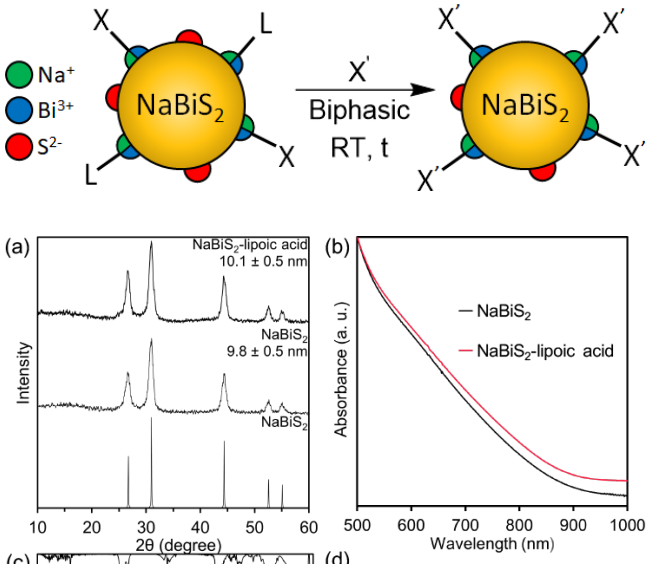

Figure 6. (a) Powder XRD, (b) solution-phase absorption spectra, and (c) IR spectra of $NaBiS_2$ nanocrystals before and after photochemical ligand exchange with lipoic acid. (d) Upon exchange, the nanocrystals transfer from the hexanes phase to methanol.

Based on these ideas, we explored a ligand exchange approach to modify the surface of colloidal $NaBiS_2$ nanocrystals (Scheme 2). Our work shows that the native oleylamine and neodecanoate ligands can be exchanged with lipoic acid using light-promoted biphasic ligand exchange (Figure 6 and SI). The structural and optical properties of the $NaBiS_2$ nanocrystals are unaffected by this procedure. After biphasic ligand exchange, $NaBiS_2$ nanocrystals lack the IR bands that are characteristic of surface-bound amine and carboxylate ligands (see above). Instead, new carboxylate stretching bands, $\nu_{as}(COO^-)$ and $\nu_s(COO^-)$, separated by 228 cm^{-1} indicate the presence of free (η^1) protonated carboxylic acid pendant groups from thiolate-bound lipoic acid ligands (see above).[50,49] This is consistent with the observation that, upon treatment with aqueous 0.1 M *t*-BuOK, the solubility of these nanocrystals in polar protic solvents (MeOH, H_2O) dramatically increases, likely due to deprotonation and formation of multiple free pendant carboxylate groups per particle. The IR spectrum also shows a ν(C-S) stretching band at ~600 cm^{-1} that is consistent with the presence of thiolate, a stronger X-type ligand, directly bonded to the nanocrystal surface. More may be learned by considering the implications of hard soft acid base (HSAB) theory in this system.[69] While sodium cations (Na^+) are hard acids, bismuth cations (Bi^{3+}) are intermediate or borderline soft/hard acids. Because thiolate anions (RS^-) are soft bases, the observed preference of lipoic acid to bind through sulfur suggests that the $NaBiS_2$ nanocrystal surface may be richer in Bi- than in Na-based cations, at least at the range of sizes analyzed here.

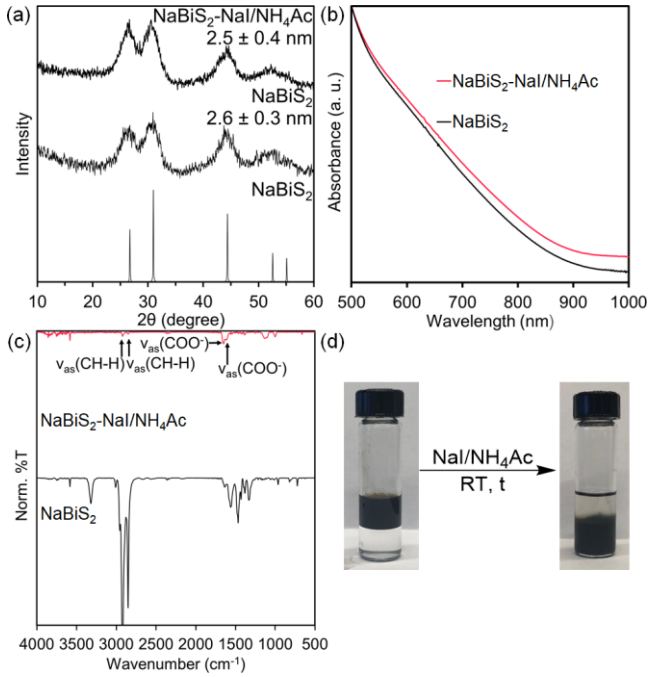

Figure 7. (a) Powder XRD, (b) solution-phase absorption spectra, and (c) IR spectra of $NaBiS_2$ nanocrystals before and after treatment with 0.1 M NaI and 0.04 NH_4Ac in DMF. (d) Upon exchange, the nanocrystals transfer from the lighter hexane (top layer) into the heavier DMF (bottom layer). In (a), very subtle changes in XRD peak intensities may be due to preferred orientation of the nanocrystal grains upon sample preparation.

For $NaBiS_2$ nanocrystals to be most immediately useful in optoelectronic devices, one must first replace long-chain insulating ligands with smaller and/or conductive inorganic ligands.[16,19,20,33,42,64,70] To do this, one commonly employed method with binary nanocrystals is a liquid-liquid biphasic ligand exchange where nanocrystals capped with long-

chain native ligands suspended in hexane are treated with short inorganic capping ligands dissolved in a polar solvent. Upon shaking, the nanocrystals phase transfer from the hexanes layer into the immiscible polar layer. We find that mixing as-made, colloidal $NaBiS_2$ nanocrystals in hexanes with 0.1 M NaI in dimethylformamide (DMF) leads to phase transfer after 5–10 min (Figure 7). A recent report showed that addition of NH_4Ac to metal halide solutions in DMF assists in faster and more complete ligand exchange.[71] Indeed, here we find that when 0.04 M NH_4Ac is added to 0.1 M NaI in DMF, phase transfer occurs almost instantaneously, within only 3 s. Importantly, $NaBiS_2$ nanocrystals are resilient to this biphasic ligand exchange, with no measurable change in their XRD size or optical properties after the process is complete (Figure 7 and SI). We considered the possibility that NaI, a rock salt material, could form during this process.[72,73,74,75] However, XRD failed to detect the formation of such impurity. Further, the IR and ^{1}H NMR spectra of $NaBiS_2$ nanocrystals treated with NaI and NaI/NH_4Ac is consistent with the complete removal of oleylamine and carboxylate ligands after this treatment.

To confirm these results, we collected dynamic light scattering (DLS) measurements of the as-made, lipoic acid-capped, and NaI/NH_4Ac-capped $NaBiS_2$ nanocrystals (see SI). Typically, the use of EtOH or MeOH as the crashing solvent results in significant aggregation of the nanocrystals well beyond their Scherrer size of 2.5±0.3 nm. Using lipoic acid as the exchange ligand, the nanocrystals did not aggregate any further. In contrast, using NaI/NH_4Ac did result in aggregation with a new distribution closer to ≈390 nm. This suggest that the exchange with NaI/NH_4Ac in DMF is a much harsher ligand exchange protocol that results in exposing highly energetic facets that neck and further aggregate.

Solid-liquid biphasic exchange: Iodide-capped $NaBiS_2$ nanocrystals. A more specific method to produce conducting nanocrystal films is multistep layer-by-layer (LbL) approach.[42,76] Each one of these steps or cycles involves spin-coating a thin nanocrystal film with native organic ligands onto a substrate, soaking this film in a ligand exchange solution, rinsing, and drying (Scheme 3). The thickness of the active layer is controlled by varying the number LbL cycles. This method allows native ligands to be exchanged without redispersing or losing nanocrystals into solution. The effectiveness of exchange normally depends on the chelating strength of the native ligands and the initial thickness of each nanocrystal film. Thicker films can limit the efficiency of ligand exchange. Several record power conversion efficiency quantum dot devices were fabricated by this method including $CsPbI_3$-[77] and PbS-based[78] solar cells.

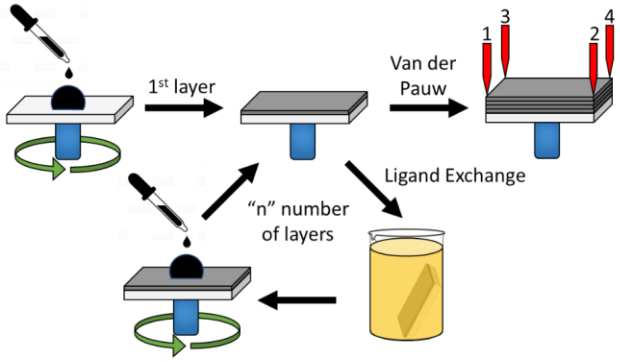

Scheme 3. Illustration of solid-liquid ligand exchange performed by the layer-by-layer (LbL) method.

We find that our ligand exchange solutions are also sufficient to fabricate conducting $NaBiS_2$ films by the LbL approach. One LbL cycle involves spin-coating a film of 5.2 ± 0.5 nm $NaBiS_2$ nanocrystals and then soaking this film in a ligand exchange solution (Scheme 3). For every two LbL cycles, the film thickness increases by 15 ± 2.0 nm (Figure 8). Soaking $NaBiS_2$ films in 0.1 M NaI and 0.04 M NH_4Ac in DMF leads to a substantial decrease in the intensity of vibrational modes corresponding to native carboxylate and amine ligands as shown by IR (see SI).

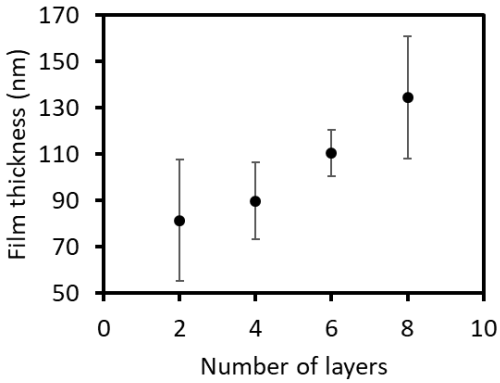

Figure 8. Film thickness of $NaBiS_2$ films as a function of layer-by-layer (LbL) NaI/NH_4Ac-treating cycles. Standard deviation was determined by 3 measurements using a profilorimeter.

X-ray photoelectron spectroscopy (XPS) of the $NaBiS_2$ films shows the disappearance of the nitrogen (N) signal from oleylamine ligands and the appearance of iodine (I) upon ligand exchange (Figure 9). Both the Na and Bi peaks shift to higher binding energies after ligand exchange, which is consistent with removal of electron density from the metal as a result of stronger passivation with iodide.[1, 79, 80] Interestingly, halide treatment also successfully suppresses the presence of surface oxidized sulfur (S). Further, XPS data shows the relative energies of the conduction and valence bands relative to the Fermi-level (Figure 10). Native $NaBiS_2$ nanocrystals are p-type semiconductors with an excess of holes. After NaI/NH_4Ac treatment, iodide-capped $NaBiS_2$ nanocrystal films acquire a more extrinsic behavior.

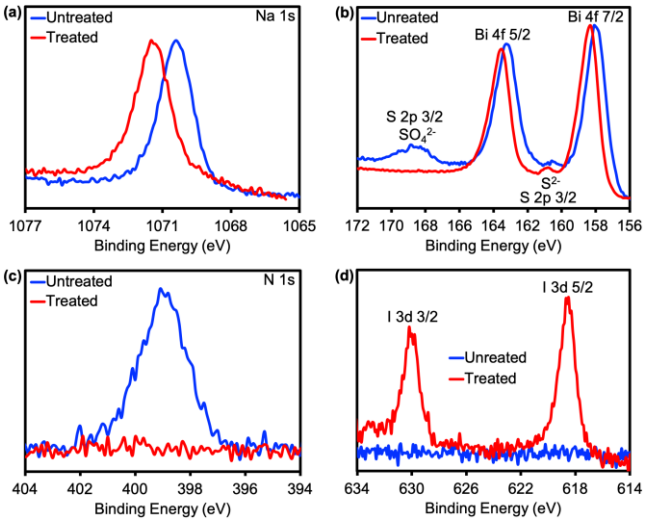

Figure 9. XPS data of $NaBiS_2$ films before (blue) and after (red) ligand exchange with 0.1 M NaI and 0.04 M NH_4Ac in DMF. (a) Na 1s region, (b) Bi 4f and S 2p regions, (c) N 1s region, and (d) I 3d region.

Making conductive $NaBiS_2$ nanocrystal films. To demonstrate the versatility of $NaBiS_2$ nanocrystal films for optoelectronic device applications,[1,4,6,8] we tested the effect of several different salt/halide treatments on film resistivity. Measurements were performed by the van der Pauw method using a square geometry with the electrodes spaced apart 25 cm or 12.5 cm (Figure 11). Conductivity values (S cm^{-1}) were calculated based on film thickness and sheet resistance (R_S). Initially, as-deposited (untreated) $NaBiS_2$ nanocrystal films capped by long-chain native ligands were found—as expected—to be completely insulating. More specifically, the sheet resistance of untreated samples and those treated with only 2 LbL cycles was beyond the detection limit of our potentiostat (Table 1). However, with increasing film thickness—*i.e.*, with increasing number of LbL cycles—we were able to detect and measure the conductivity of the treated $NaBiS_2$ nanocrystal films. In particular, films treated with six (6) NaI/NH_4Ac LbL cycles gave the best conductivity measurements. After eight (8) LbL cycles, the conductivity decreased again, indicating that the optimal number of LbL treatment cycles had been reached.

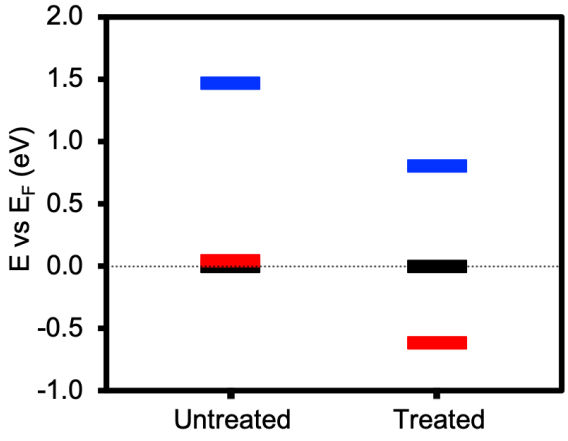

Figure 10. Relative valence band (red) and conduction band (blue) positions in respect to Fermi-level (black) of untreated and NaI/NH_4Ac-treated $NaBiS_2$ nanocrystals.

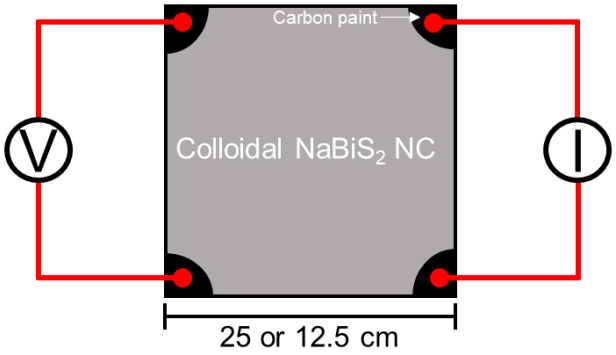

Figure 11. Van der Pauw set up used to measure the conductivity of $NaBiS_2$ nanocrystal films treated with different salt solutions.[81]

Various halide salts were used to replace the native ligands on the surface of $NaBiS_2$ nanocrystals by biphasic solid-liquid exchange (Table 2). In comparison to our best NaI/NH_4Ac-based treatment, others treatments such as that based on NaCl/NH_4Ac resulted in films that peeled and degraded in the ligand exchange solution. Only a 12.5 cm × 12.5 cm film could be recovered and measured. In the end, the conductivity of the best iodide-capped $NaBiS_2$ nanocrystal films presented here is in the same order of magnitude and comparable to that observed for plasma-treated isostructural, rock salt PbS nanocrystal films (Table 2) (for comparison, the single crystal conductivity of PbS ranges between 0.11 to 1800 S cm^{-1}).[82] Further improvements in conductivity could be achieved by additional nanostructuring or doping strategies, or by using mixed metal chalcogenides.

Table 1. Electronic properties of films made with NaI/NH_4Ac-treated $NaBiS_2$ nanocrystals.

Number of LbL Cycles[a]	Thickness (nm)[b]	$R_s \times 10^9$ ($\Omega/\square$)[c]	Conductivity $\times 10^{-4}$ (S cm^{-1})
Untreated	0	-[d]	-
2	81±26	-[d]	-
4	90±16	136	0.0122±0.0024
6	110±10	8.63	1.48±0.22
8	135±26	8.99	0.121±0.024

[a]$NaBiS_2$ (5.2±0.5 nm) in toluene (30 mg/mL) used as ink. [b]From profilometry. [c]Van der Pauw method. [d]Sheet resistance larger than potentiostat detection limit. Standard deviations from 3 separate measurements.

Finally, we fabricated solar cells based from PbX_2-treated $NaBiS_2$ nanocrystals (X = Br, I) using the device architecture shown in Figure 12. Focused ion beam scanning electron microscopy (FIB-SEM) shows the high quality of the multilayer structure, as well as Pb-incorporation into the active layer (see SI). Under AM 1.5G illumination, our best solar cell device—made with 4 LbL cycles—exhibited a power

conversion efficiency (PCE) of 0.07 % and no hysteresis, with a J_{SC} of 0.18± 0.01 mA/cm^2, V_{OC} of 638±7 mV, and *FF* of 56±3. Statistical analysis of this multilayer structure over 9 pixels gave a 624±30 mV, a J_{SC} of 0.17±0.01 mA/cm^2, a *FF* of 53±5, and a PCE of 0.06±0.01 %. Our V_{OC} and *FF* values are comparable to those of state-of-the-art PbS quantum dot solar cells,[83] which exhibit a V_{OC} of 611 mV and a *FF* of 68 %.[71] Because PCE = $J_{sc} \times V_{oc} \times FF$, our much lower J_{SC} value—compared to that of 27.23 mA/cm^2 observed for PbS—is responsible for the low PCE we observed. At present, we strongly suspect this may be caused by the $NaBiS_2$ nanocrystal films behaving mainly as an indirect band gap semiconductor, which may limit the efficiency of charge generation and collection.[9] Nonetheless, we believe these results are very encouraging. Future work will pursue further improvements—through doping, nanostructuring, surface passivation, and/or additional ligand optimization—in order to engender direct band gap character and increase the efficiency of $NaBiS_2$ nanocrystal-based devices.

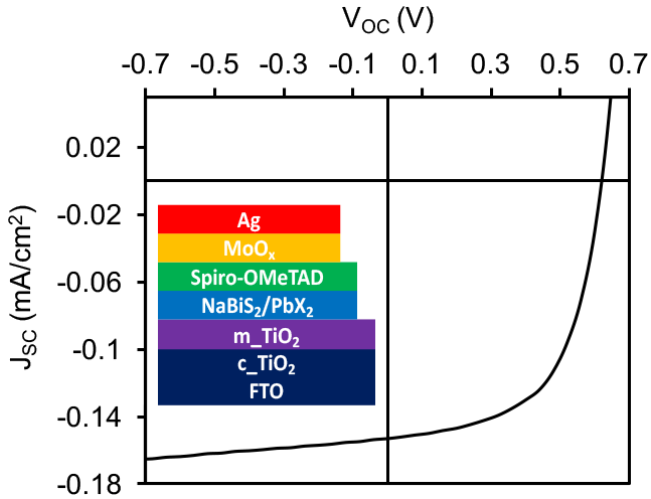

Figure 12. Representative *J*–*V* curve of PbX_2-treated (X=Br, I) (4 LbL) $NaBiS_2$ nanocrystal solar cells (see Experimental). The device parameters were measured under AM 1.5G illumination. Average device parameters were determined over 9 pixels with V_{OC} of 624±30 mV, a J_{SC} of 0.17±0.01 mA/cm^2, a *FF* of 53±5, and a PCE of 0.06±0.01 %.

Table 2. Properties of $NaBiS_2$ nanocrystal films treated for 6 LbL cycles with different halide salts.

Salt[a]	Thickness (nm)[b]	25×25 cm R_s (Ω / □)[c]	12.5×12.5 cm R_s (Ω / □)[c]	Conductivity 25×25 cm (S cm^{-1})	Conductivity 12.5×12.5 cm (S cm^{-1})
NaI	110±10	1.66×10^{13}	8.63×10^{9}	$(1.83\pm0.16) \times 10^{-8}$	$(9.49\pm0.55) \times 10^{-4}$
NaCl	171±10	-[d,e]	1.93×10^{11}	-	$(3.31\pm0.18) \times 10^{-6}$
KBr	175±26	8.66×10^{10}	8.66×10^{9}	$(1.52\pm0.22) \times 10^{-6}$	$(1.48\pm0.22) \times 10^{-5}$
NaBr	116±10	9.56×10^{10}	9.31×10^{9}	$(1.11\pm0.09) \times 10^{-6}$	$(1.08\pm0.09) \times 10^{-5}$
TMAI[e]	114±10	2.44×10^{11}	9.42×10^{9}	$(2.79\pm0.24) \times 10^{-6}$	$(1.08\pm0.24) \times 10^{-5}$
KI	141±12	9.35×10^{10}	9.59×10^{9}	$(1.32\pm0.11) \times 10^{-6}$	$(1.36\pm0.11) \times 10^{-5}$

[a]6 LbL cycles of 30 mg/mL $NaBiS_2$ (5.2±0.5 nm) in toluene used as ink. [b]From profilometry. [c]Measured by the Van der Pauw method. [d]Sheet resistance larger than potentiostat detection limit. [e]Film peeled off; not measured. [e]Ligand exchange solution made in MeOH. Standard deviations from 3 separate measurements.

Conclusions

We have demonstrated that colloidal $NaBiS_2$ nanocrystals can be easily made from Earth abundant, cheap, and relatively non-toxic precursors. The size of the nanocrystals is easily manipulated by controlling the growth temperature during synthesis, resulting in a small standard deviation in crystallite size. We have probed the surface chemistry of these complex ternary $NaBiS_2$ nanocrystals using IR and ^{1}H NMR. As-made colloidal $NaBiS_2$ nanocrystals have L-type (oleylamine) and X-type (η^2-bound neodecanoate) ligands attached to cationic sites on their surface. Removal of the native X- and L-type ligands with lipoic acid or halide ligands can be achieved through a liquid-liquid biphasic ligand exchange. The resulting nanocrystals become soluble in polar solvents, like methanol or water, yet retain their structure, optical properties, and colloidal stability.

To capitalize on this newly acquired knowledge, we explored a layer-by-layer (LbL) solid-liquid approach to exchange the native ligands starting from $NaBiS_2$ nanocrystal films. As the number of LbL cycles increases, the size of the thin film increases—by 15±2.0 nm for every two cycles—reaching an optimum minimum resistivity after 6 LbL cycles. In addition to the disappearance of the native ligands as observed by IR, XPS also shows the disappearance of nitrogen (N, from oleylamine), appearance of iodine (I), and a shift in Na and Bi binding energy to higher eV. Further, while as-made $NaBiS_2$ nanocrystal films have p-type semiconductor character, the iodide-exchanged films have more intrinsic behavior. To further elucidate the capabilities of these thin films, various halide ligand salts—iodide, bromide, chloride—were used as the capping ligand. The best con-

ductivity measured was for iodide-capped $NaBiS_2$ nanocrystal films, and is comparable in magnitude to that previously observed for isostructural PbS quantum dots.

Finally, we prepared the first photovoltaic devices made of $NaBiS_2$ nanocrystals treated with PbX_2 (X = Br, I) as the exchange ligands. FIB-SEM showed the incorporation of Pb into the active layer of the multilayer structure. Our best device used 4 LbL cycles, yielding a J_{SC} of 0.18± 0.01 mA/cm^2, a V_{OC} of 638±7 mV, a *FF* 56±3, and a modest PCE of 0.07 %. Efforts are under way to further enhance the PCE of similar devices by nanostructuring and further ligand exchange/coverage optimization, thus allowing for better charge separation and a higher J_{sc} value. Together, these results demonstrate the potential role and utility of non-toxic, Earth abundant, and air stable $NaBiS_2$ nanocrystals to play a new role in photovoltaic and other energy conversion applications.

Experimental

Materials. Oleylamine (oleylNH_2, technical grade, 70%) and bismuth(III) neodecanoate, ammonium acetate (NH_4Ac, > 97%), N,N-dimethylformamide (>99%) , tetramethylammonium iodide (TMAI, 99%), lipoic acid (LA, 98%), lead iodide (PbI_2, 99%), 4-*tert*-butylpyridine (TBP, 96%), chlorobenzene (anhydrous, 98.8%), titanium diisopropoxide bis(acetylacetonate) (75 wt% in isopropanol), titanium(IV) ethoxide (technical grade), isopropyl alcohol (IPA, ≥99.5%), acetone (≥99.5%), potassium *tert*-butoxide (*t*-BuOK, >98%), lithium bistrifluoromethanesulfonimidate (99%), and acetonitrile (anhydrous, 98%) were purchased from Sigma-Aldrich; sodium oleate (99%) from Strem; sulfur (99.999%), sodium iodide (NaI, 99.9%), and potassium iodide (KI, 99%) from Alfa Aesar; toluene (99.9%), hexanes (99.9%), methanol (99.9%), sodium bromide (NaBr, 99.5%), potassium bromide (KBr, 99.9%), hydrochloric acid (HCl, 36.9%), and sodium chloride (NaCl, 99.8%) from Fisher; lead bromide ($PbBr_2$, 98%) and molybdenum oxide (MoO_3, 99%) from Acros Organics; 2,2',7,7'-tetrakis(N, N-di-p-methoxyphenylamino)-9,9'-spiroobifluorene (spiro-OMeTAD, 99%) from Lumtec; titanium dioxide paste (TiO_2) from Dyesol; carbon paint from Ted Pella; and silver (Ag, 99.999%) from Kurt J. Lesker. All chemicals were used as received.

Synthesis. *Bismuth(III) neodecanoate stock solution.* Bismuth(III) neodecanoate (0.7 mL) was added to oleylamine (9.3 mL) and the solution was stirred at room temperature until it became homogeneous (~10–20 min). *$NaBiS_2$ synthesis.* Sodium oleate (0.11 mmol, 35 mg), bismuth(III) neodecanoate stock solution (0.11 mmol Bi, 1 mL), S (0.22 mmol, 7.3 mg), and degassed oleylamine (4 mL) were stirred at 60 °C for 30 min, heated between 100–250 °C for 2 h (see discussion above and SI), and cooled to RT by removal from the heating mantle. *Purification.* The crude solution was diluted to 15 mL with methanol or ethanol, centrifuged at 4500 rpm for 3 min, and the supernatant discarded. The precipitate was then suspended in toluene or hexanes.

Biphasic Ligand Exchange. *Stock solution of 0.1 M NaI + 0.04 M NH_4Ac in DMF.* NaI (1 mmol, 149.9 mg) and NH_4Ac (0.4 mmol, 30.8 mg) were added to DMF (10 mL) and then sonicated until dissolved. *Stock solution of 0.1 M NaI.* NaI (1 mmol, 149.9 mg) was added to DMF (10 mL) and then sonicated until dissolved. *Biphasic ligand exchange.* Equal parts $NaBiS_2$ in hexanes and the desired ligand exchange solution were added to a centrifuge tube that was vortexed until complete phase transfer of $NaBiS_2$ from the hexanes layer (top) to the DMF layer (bottom). The hexanes layer was decanted and then the DMF layer was washed two more times with hexanes. The DMF layer was centrifuged at 4500 rpm for 5 min to precipitate $NaBiS_2$ nanocrystals. The pellet was resuspended in DMF for further measurements. *Lipoic acid exchange.* Lipoic acid (0.3 mmol, 60 mg) was added to TMAH stock solution (1 mL)[65] in a 3 mL cylindrical glass flask with a Teflon stir bar. Washed (1× with ethanol) $NaBiS_2$ nanocrystals (10 mg/mL, 1 mL) in hexanes were added to the flask, followed by UV-radiation for 30 min while stirring at 450 rpm. The solution was transferred to a centrifuge tube and centrifuged for 5 min at 4500 rpm. The supernatant was decanted and 3 mL of hexanes and MeOH was added, the mixture then centrifuged for 5 min at 4500 rpm. The solvent was decanted and dried for 20 min under dynamic vacuum. The crystals were dissolved using 5 mL of 0.1 M *t*-BuOK in deionized water. *Solid-liquid biphasic ligand exchange. Stock solution of 0.1 M NaI + 0.04 M NH_4Ac.* NaI (1 mmol, 0.1499 g) and NH_4Ac (0.4 mmol, 0.0308 g) were added to DMF (10 mL) and then sonicated until dissolved. Glass microscope slides were cleaned by ultrasonication in 1% Alconox soap water and isopropanol for 15 min each and dried with nitrogen. The slides were then cleaned under O_2 plasma for 10 min. Glass microscope slides were kept in the glovebox until further use. A film of $NaBiS_2$ was deposited using six cycles of the layer-by-layer (LbL) process using a 30 mg/mL solution of 5.2 ± 0.5 nm $NaBiS_2$ nanocrystals in toluene filtered through a 0.1 μm polytetrafluoroethylene (PTFE) filter. One LbL cycle involved completely covering the glass substrate with $NaBiS_2$ solution, spinning the substrate at 2000 rpm for 30 s, and submerging the $NaBiS_2$-covered substrate in the ligand exchange solution for 1 min. The substrates were rinsed in neat DMF followed by toluene and then blown dry with N_2. Thicker or thinner films were made by performing more or fewer LbL cycles. The treated substrates were then annealed in air at 100 °C for 5 min. NaCl, KBr, NaBr, and KI can be substituted for NaI with 1 mmol and 0.04 M NH_4Ac in 10 mL of DMF. TMAI/NH_4Ac was dissolved in methanol instead of DMF.

Structural and Compositional Characterization. *Powder X-ray diffraction* patterns were measured using Cu Kα radiation on a Rigaku Ultima IV (40 kV, 44 mA) diffractometer using a background-less quartz sample holder. Scherrer analysis was performed with Jade using a κ value of 0.9. *Transmission Electron Microscopy* imaging was performed on a FEI Tecnai G2-F20 scanning transmission electron microscope. *X-ray photoelectron spectroscopy (XPS)* measurements were performed using a Kratos Amicus/ESCA 3400 instrument. The sample was irradiated with 240 W unmonochromated Mg *Kα* x-rays, and photoelectrons emitted at 0° from the surface normal were energy analyzed using a DuPont type analyzer. The pass energy was set at 150 eV and a Shirley baseline was removed from all reported spectra. CasaXPS was used to process raw data files. *Focused Ion Beam Scanning Electron Microscopy (FIB-SEM)* measurements were performed on a FEI Helios DualBeam FIB/SEM

system was used that combines sputtering, imaging, and analytical capabilities. A beam of gallium ions was used for nm precision milling and imaging down to 5 nm resolution levels. The system also enables Energy-dispersive X-ray spectroscopy (EDS).

Spectroscopic Characterization. *Solution absorbance* spectra were measured with a photodiode array Agilent 8453 UV-Vis spectrophotometer with solvent absorption (toluene or DMF) subtracted from all spectra. *Band gap values* were estimated by extrapolating the linear slope of Tauc plots by plotting $(Ah\nu)^{1/r}$ *vs.* hν where A = absorbance, hν = incident photon energy in eV, r = ½ for direct and r = 2 for indirect semiconductors. *Dynamic light scattering* (DLS) were measured with a Malvern Zetasizer Nano ZS equipped with a 532 nm laser. Square glass cells with a 12mm (outer diameter) were used for all measurements. *Infrared (IR) spectroscopy* measurements were performed on a Bruker Tensor 37 Fourier transform IR spectrophotometer (16 scans, transmittance mode, 4 cm^{-1} resolution). *^{1}H nuclear magnetic resonance (NMR) spectroscopy* measurements were performed on a Bruker Avance III 600 MHz NMR spectrometer (32 scans). Deuterated chloroform was used for as-synthesized $NaBiS_2$ nanocrystals while deuterated DMF was used for $NaBiS_2$ treated with NaI or NaI/NH_4Ac.

Conductivity Measurements. Film conductivity was measured using the Van der Pauw method[81] with thin $NaBiS_2$ nanocrystal films of known thickness in a square geometry with corner contacts (see Figure 11 above). The corners were contacted with carbon paint and probed using micromanipulated probes on a home-build probe station. A Keithley 2400 in four-wire source-sense mode was used to simultaneously source current and measure voltages. Sheet resistances were determined by numerical integration. Reported values are the average of several measurements ranging over several orders of magnitude of source current.

Solar Cell Fabrication and Testing. *Glass substrate cleaning and preparation.* FTO Hartford Glass, Tec 7, 25 mm × 25 mm × 2.2 mm, 6-8 ohm/sq) glass substrates were cleaned by sonicating in Decon™ Contrex™ AP Labware Detergent solution in DI water (1%) for 20 min under mild heat (~50 °C). The substrates were thoroughly rinsed in DI water and sonicated for another 20 min in DI water under mild heat. The substrates were rinsed once more with DI water, sonicated in acetone for 20 min, and isopropyl alcohol for 20 min. The FTO substrates were rinsed once more DI water, blown dry with N_2, and treated with O_2 plasma for 20 min. The unused substrates were stored in a dry N_2-filled glovebox until further use. *Solution deposition of TiO_2.* TiO_2 was deposited using 0.210 mL of HCl, 30.4 mL of ethanol, 2.21 mL of titanium(IV) ethoxide. The solution was vigorously stirred and sonicated for 30 min. The solution was filtered through a 0.45 μm PTFE filter, and deposited on to freshly cleaned FTO and placed in a spincoater. The spincoater lid was closed, and the sample was spun at 2000 rpm for 35 s. FTO contact points were made by wiping the spincoated film with an ethanol-coated swab. The FTO substrates were annealed at ~500 °C on a hot plate for 30 min. The substrates were allowed to cool naturally and stored in a dry N_2-filled glove box until further use. *Solution deposition of mesoporous TiO_2 (m-TiO_2)*. TiO_2 paste (4.5 g) was dissolved in ethanol (20 mL), and sonicated for 45 min until completely dissolved. m-TiO_2 solution (200 μL) was deposited onto c-TiO_2 coated substrate and spin coated at 3000 rpm for 30 s. After spin coating, the glass substrates were annealed at ~450 °C for 30 min, cooled to RT, and stored in a dry N_2-filled glovebox until further use. *NaBiS2 active layer.* As described previously (see above), a solution of $NaBiS_2$ nanocrystals (30 mg/mL) was prepared by washing the crude material with ethanol, centrifuging for 5 min at 4500 rpm, and drying for 20 min under dynamic vacuum. The nanocrystals were resuspended in toluene and filtered through a 0.1 μm PTFE filter. $NaBiS_2$ nanocrystals (30 mg/mL, 100 μL) were deposited on FTO substrates and spun at 2000 rpm for 30 s. The freshly deposited substrate was dipped in a ligand exchange solution containing in $PbBr_2$ (0.1 M, 1.83 g), PbI_2 (0.04 M, 0.992 g), and NH_4Ac (0.04 M, 154 mg) in DMF (50 mL) for 20-25 s. After repeating for the number of desired LbL cycles, the substrates were rinsed in neat DMF for 20-25 s, toluene for 20-25 s, and blown dried with N_2 gas. *Spiro-OMeTAD layer.* 2,2',7,7'-tetrakis(N, N-di-p-methoxyphenylamino)-9,9'-spiroobifluorene (spiro-OMeTAD) (72 mg, 0.06 mmol), 4-*tert*-butylpyridine (TBP, 29.8 μL), and a solution of lithium bistrifluoromethanesulfonimidate in acetonitrile (520 mg/mL, 17.5 μL) were dissolved in chlorobenzene (1 mL). The combined spiro-OMeTAD solution was spin coated onto the $NaBiS_2$ active layer at 3000 rpm for 30 s. *MoO_3 and Ag layers.* MoO_3 (15 nm) and Ag (100 nm) were thermally evaporated directly onto the spiro-OMeTAD film through a shadow mask—9 circular 8 mm^2 holes arranged in a 3×3 square array—at a base pressure of 2×10^{-6} mbar. *Power conversion efficiency* (PCE) of photovoltaic devices was determined using current−voltage (J−V) characterization under solar simulation (Newport, M-9119X with an AM1.5G filter). The intensity was adjusted to 100 mW/cm^2 using an NREL-certified Hamamatsu mono-Si photodiode (S1787−04). A calibrated Si photodiode with a known spectral response spectrum was used as a reference and all measurements were taken under N_2.

ASSOCIATED CONTENT

Supporting Information

UV-Vis absorption, IR, ^{1}H NMR, and XPS spectra, TEM and SEM images of particles and nanocrystal films, profilometry and DLS data, and solar cell device images. The Supporting Information is available free of charge on the ACS Publications website.

AUTHOR INFORMATION

Corresponding Author

* vela@iastate.edu

Present Addresses

†Center for Chemistry and Nanoscience, National Renewable Energy Laboratory, 15013 Denver West Parkway, Golden, CO 80401, USA.

ACKNOWLEDGMENT

J.V. gratefully acknowledges the U.S. National Science Foundation for a grant from the Division of Chemistry, Macromolecular, Supramolecular, and Nanochemistry Program (1905066).

We thank Sarah Cady and Matthew Lynn for assistance with solution phase NMR and TEM measurements, respectively.

REFERENCES

(1) Bernechea, M.; Miller, N. C.; Xercavins, G.; So, D.; Stavrinadis, A.; Konstantatos, G. Solution-Processed Solar Cells Based on Environmentally Friendly $AgBiS_2$ Nanocrystals. *Nat. Photon.* **2016,** *10*, 521–525.
(2) Fabini, D. H.; Koerner, M.; Seshadri, R. Candidate Inorganic Photovoltaic Materials from Electronic Structure-Based Optical Absorption and Charge Transport Proxies. *Chem. Mater.* **2019,** *31*, 1561–1574.
(3) Rahayu, S. U.; Chou, C.-L.; Suriyawong, N.; Aragaw, B. A.; Shi, J.-B.; Lee, M.-W. Sodium Antimony Sulfide ($NaSbS_2$): Turning an Unexpected Impurity into a Promising, Environmentally Friendly Novel Solar Absorber Material. *APL Mater.* **2016**, *4*, 116103-1 116103-7.
(4) Roychowdhury, S.; Panigrahi, R.; Perumal, S.; Biswas, K. Ultrahigh Thermoelectric Figure of Merit and Enhanced Mechanical Stability of p-Type $AgSb_{1-x}Zn_xTe_2$. *ACS Energy Lett.* **2017**, 349–356.
(5) Sun, J.; Singh, D. J. Electronic Properties, Screening, and Efficient Carrier Transport in $NaSbS_2$. *Phys. Rev. App.* **2017**, *7,* 024015-1–024015-6.
(6) Yang, C.; Wang, Z.; Wu, Y.; Lv, Y.; Zhou, B.; Zhang, W.-H. Synthesis, Characterization, and Photodetector Application of Alkali Metal Bismuth Chalcogenide Nanocrystals. *ACS Appl. Energy Mater.* **2019**, *2*, 182–186.
(7) Xiaa, Z.; Yua, F.-X.; Lua, S.-C.; Xueb, D.-J.; Hea, Y.-S.; Yanga, B.; Wanga, C.; Dinga, R.-Q.; Zhongc, J.; Tang, J. Synthesis and Characterization of $NaSbS_2$ Thin Film for Potential Photodetector and Photovoltaic Application. *Chinese Chem. Lett.* **2017***, 28,* 881–887.
(8) Fei, H. L.; Feng, Z. W.; Liu, X. Novel Sodium Bismuth Sulfide Nanostructures: A Promising Anode Materials for Sodium-Ion Batteries with High Capacity. *Ionics* **2015,** *21*, 7, 1967–1972.
(9) Rosales, B. A.; White, M. A.; Vela, J. Solution-Grown Sodium Bismuth Dichalcogenides: Toward Earth-Abundant, Biocompatible Semiconductors. *J. Am. Chem. Soc.* **2018,** *140*, 10, 3736-3742.
(10) Lin, Q.; Yun, H. J.; Liu, W.; Song, H.-J.; Makarov, N. S.; Isaienko, O.; Nakotte, T.; Chen, G.; Luo, H.; Klimov, V. I.; Pietryga, J. M. Phase-Transfer Ligand Exchange of Lead Chalcogenide Quantum Dots for Direct Deposition of Thick, Highly Conductive Films. *J. Am. Chem. Soc.* **2017,** *139*, 19, 6644–6653.
(11) Dasong, M.; Kehrle, J.; Rieger, B.; Veinot, C. G. J. Silicon Nanocrystals and Silicon-Polymer Hybrids: Synthesis, Surface Engineering, and Application. *Angew. Chem. Int. Ed.* **2016**, *55*, 2322–2339.
(12) Hanrahan, P. M.; Fought, L. E.; Windus, L. T.; Wheeler, M. L.; Anderson, C. A.; Neale, R. N.; Rossini, J. A. Characterization of Silicon Nanocrystals Surfaces by Multidimensional Solid-State NMR Spectroscopy. *Chem. Mater.* **2017**, *29*, 10339–10351.
(13) Muthuswamy, E.; Zhao, J.; Tabatabaei, K.; Amador, M. M.; Holmes, A. M.; Osterloh, E. F.; Kauzlarich, M. S. Thiol-Capped Germanium Nanocrystals: Preparation and Evidence for Quantum Size Effects. *Chem. Mater.* **2014**, *26*, 2138–2146.
(14) Wheeler, L. M.; Nichols, A. W.; Chernomordik, B. D.; Anderson, N. C.; Beard, M. C.; Neale, N. R. All-Inorganic Germanium Nanocrystal Films by Cationic Ligand Exchange. *Nano Lett.* **2016**, *16*, 1949–1954.
(15) Kuno, M.; Lee, K. J.; Dabbousi, O. B.; Mikulec, V. F.; Bawendi, G. M. The Band Edge Luminescence of Surface Modified CdSe Nanocrystallites: Probing the Luminescing State. *J. Chem. Phys.* **1997**, *106*, 9869–9882.
(16) Kovalenko, V. M.; Scheele, M.; Talapin, V. D.; Colloidal Nanocrystals with Molecular Metal Chalcogenide Surface Ligands. *Science* **2009**, *324*, 1417–1420.
(17) Kagan, C. R.; Murray, C. B. Charge Transport in Strongly Coupled Quantum Dot Solids. *Nat Nanotechnol* **2015,** *10*, 12, 1013–1026.
(18) Brown, R. P.; Kim, D.; Lunt, R. R.; Zhao, N.; Bawendi, G. M.; Grossman, C. J.; Bulovic, V. Energy Level Modification in Lead Sulfide Quantum Dot Thin Films through Ligand Exchange. *ACS Nano* **2014**, *8*, 5863–5872.
(19) Boles, M. A.; Engel, M.; Talapin D. V. Self-Assembly of Colloidal Nanocrystals: From Intricate Structures to Functional Materials. *Chem. Rev.* **2016**, *116*, 11220–11289.
(20) Boles, M. A.; Ling, D.; Hyeon, T.; Talapin, D. V. The Surface Science of Nanocrystals. *Nature Materials* **2016**, *15*, 141–153.
(21) Mobarok, M. H.; Buriak, J. M. Elucidating the Surface Chemistry of Zinc Phosphide Nanocrystals Through Ligand Exchange. *Chem. Mater.* **2014**, *26*, 4653–4661.
(22) Ai, K.; Liu, Y.; Liu, J.; Yuan, Q.; He, Y.; Lu, L. Large-Scale Syntehsis of Bi_2S_3 Nanodots as a Contrast Agent for In Vivo X-ray Computed Tomography Imaging. *Adv. Mater.* **2011**, *23*, 4886–4891.
(23) Thomson, J. W.; Cademartiri, L.; MacDonald, M.; Petrov, S.; Calestani, G.; Zhang, P.; Ozin, G. A. Ultrathin Bi_2S_3 Nanowires: Surface and Core Structure at the Cluster-Nanocrystal Transition. *J. Am. Chem. Soc.* **2010**, *132*, 9058–9068.
(24) Mansur, A. A. P,; Ramanery, F. P.; Oliveira, L. C.; Mansur, H. S. Carboxymethyl Chitosan Functionalization of Bi_2S_3 Quantum Dots: Towards Eco-Friendly Fluorescent Core-Shell Nanoprobes. *Carbohyd. Polym.* **2016**, *146*, 455–466.
(25) Rath, A. K.; Bernechea, M.; Martinez, L.; Garcia de Arquer, F. P.; Osmond, J.; Konstantatos, G. Solution-Processed Inorganic Bulk Nano-Heterojunctions and their Application to Solar Cells. **2012**, *6*, 529–534.
(26) Konstantatos, G.; Levina, L.; Tang, J.; Sargent, E. H.; Sensitive Solution-Processed Bi_2S_3 Nanocrystalline Photodetectors. *Nano Lett.* **2008**, *8*, 4002–4006.
(27) Cademartiri, L.; Malakooti, R.; O'Brien, P. G.; Migliori, A.; Petrov, S.; Kherani, N. P.; Ozin, G. A. Large-Scale Synthesis of Ultrathin Bi_2S_3 Necklace Nanowires. *Angew. Chem. Int. Ed.* **2008**, *47*, 3814–3817.
(28) Yao, R.-Y.; Zhou, Z.-J.; Hou, Z.-L.; Wang, X.; Zhou, W.-H.; Wu, S.-X. Surfactant-Free $CuInS_2$ Nanocrystals: An Alternative Encounter-Electrode Material for Dye-Sensitized Solar Cells. *ACS Appl. Mater. Interfaces* **2013**, *5*, 3143-3148.

(29) Kolny-Olesiak, J.; Weller, H.; Synthesis and Application of Colloidal $CuInS_2$ Semiconductor Nanocrystals. *ACS Appl. Mater. Interfaces* **2013**, *5*, 12221–12237.
(30) Dierick, R.; Van Den Broeck, F.; Nolf, K. D.; Zhao, Q.; Vantomme, A.; Martins, J. C.; Hens, Z. Surface Chemistry of $CuInS_2$ Colloidal Nanocrystals, Tight Binding of L-Type Ligands. *Chem. Mater.* **2014**, *26*, 5950–5957.
(31) Stolle, C. J.; Panthani, M. G.; Harvey, T. H. Akhaven, V. A.; Korgel, B. A. Comparison of the Photovoltaic Response of Oleylamine and Inorganic Ligand-Capped $CuInS_2$ Nanocrystals. *ACS Appl. Mater. Interfaces* **2012**, *4*, 2757–2761.
(32) Korala, L.; Braun, B. M.; Kephart, M. J.; Tregillus, Z.; Prieto, L. A. Ligand-Exchanged CZTS nanocrystals Thin Films: Does nanocrystal Surface Passivation Effectively Improve Photovoltaic Performance? *Chem. Mater.* **2017**, *29*, 6621–6629.
(33) Jiang, C.; Lee, J.-S.; Talapin, D. V.; Soluble Precursors for $CuInSe_2$, $CuIn_{1-x}Ga_xSe_2$, and $Cu_2ZnSn(S,Se)_4$ Based on Colloidal Nanocrystals and Molecular Metal Chalcogenide Surface Ligands. *J. Am. Chem. Soc.* **2012**, *134,* 5010–5013.
(34) Kim, I.; Kim, K.; Oh, Y.; Woo, K.; Cao, G.; Jeong, S.; Moon, J. Bandgap-Graded $Cu_2Zn(Sn_{1-x}Ge_x)S_4$Thin-Film Solar Cells Derived from Metal Chalcogenide Complex Ligand Capped Nanocrystals. *Chem. Mater.* **2014**, *26*, 3957–3965.
(35) Choi, H.; Kim, S.; Luther J. M.; Kim, S.-W.; Shin, D.; Beard, M. C.; Jeong, S. Facet-Specific Ligand Interactions on Ternary $AgSbS_2$ Colloidal Quantum Dots. *Chem. Eur. J.* **2017**, *23*, 17707–17713.
(36) Roo, D. J.; Ibáñez, M.; Geiregat, P.; Nedelcu, G.; Walravens, W.; Maes, J.; Martins, C. J.; Driessche, V. I.; Kovalenko, V. M.; Hens, Z. Highly Dynamic Ligand Binding and Light Absorption Coefficient of Cesium Lead Bromide Peroskite Nanocrystals. *ACS Nano* **2016**, *10*, 2071–2081.
(37) Almeida, G.; Infante, I.; Manna, L. Resurfacing Halide Perovskite Nanocrystals. *J. Am. Chem. Soc.* **2019**, *364*, 833–834.
(38) Wheeler, M. L.; Sanehira, M. E.; Marshall, R. A.; Schulz, P.; Suri, M.; Anderson, C. N.; Christians, A. J.; Nordlund, D.; Sokaras, D.; Kroll, T.; Harvery, P. S.; Berry, J. J.; Lin, Y. L.; Luther, M. J. Targeted Ligand-Exchange Chemistry of Cesium Lead Halide Perovskite Quantum Dots for High-Efficiency Photovoltaics. *J. Am. Chem. Soc.* **2018**, *140*, 10504–10513.
(39) Smock, S. R.; Williams, T. J.; Brutchey, R. L. Quantifying the Thermodynamics of Ligand Binding to $CsPbBr_3$ Quantum Dots. *Angew. Chem. Int. Ed.* **2018**, *57*, 11711–11715.
(40) Chen, Y.; Smock, S. R.; Flintgruber, A. H.; Perras, F. A.; Brutchey, R. L.; Rossini, A. J. Surface Termination of $CsPbBr_3$ Perovskite Quantum Dots Determined by Solid-Sate NMR Spectroscopy. *J. Am. Chem. Soc.* **2020**, *142*, 6117–6127.
(41) Almeida, G.; Ifante, I.; Manna, L. Resurfacing Halide Perovskite Nanocrystals. *Science* **2019**, *364*, 833–834.
(42) Boles, M. A.; Ling, D.; Hyeon, T.; Talapin, D. V. The Surface Science of Nanocrystals. *Nat. Mater.* **2016,** *15*, 2, 141–153.
(43) Ko, J. H.; Yoo, D.; Kim, Y. H. Atomic Models for Anionic Ligand Passivation of Cation-Rich Surfaces of IV-VI, II-VI, and III-V Colloidal Quantum Dots. *Chem. Commun.* **2017,** *53*, 2, 388–391.
(44) Choi, H.; Ko, J. H.; Kim, Y. H.; Jeong, S. Steric-Hindrance-Driven Shape Transition in PbS Quantum Dots: Understanding Size-Dependent Stability. *J. Am. Chem. Soc.* **2013,** *135*, 14, 5278–5281.
(45) Viñes, F.; Konstantatos, G.; Illas, F. Matildite Contact with Media: First-Principles Study of $AgBiS_2$ Surfaces and Nanoparticle Morphology. *J. Phys. Chem. B* **2018,** *122*, 2, 521–526.
(46) Green, M. L. H. A New Approach to the Formal Classification of Covalent Compounds of the Elements. *J. Organomet. Chem.* **1995**, *500*, 127–148.
(47) Owen J. The Coordination Chemistry of Nanocrystal Surfaces. *Science* **2015**, *347*, 615–616.
(48) Thomson, W. J.; Nagashima, K.; Macdonald, M. P.; Ozin, A. G. From Sulfur–Amine Solution to Metal Sulfide Nanocrystals: Peering into the Oleylamine–Sulfur Black Box. *J. Am. Chem. Soc.* **2011**, *133*, 5036–5041.
(49) Tavasoli, E.; Guo, Y.; Kunal, P.; Grajeda, J.; Gerber, A.; Vela, J. Surface Doping Quantum Dots with Chemically Active Native Ligands: Controlling Valence without Ligand Exchange. *Chem. Mater.* **2012**, *24*, 4231–4241.
(50) Zelenak, V.; Vargova, Z.; Gyoryova, K. Correlation of Infrared Spectra of Zinc(II) Carboxylates with their Structures. *Spectrochim. Acta. A* **2007**, *66*, 262–272.
(51) Zhang, J.; Zhang, H.; Cao, W.; Pang, Z.' Li, J.' Shu, Y.; Zhu, C.; Kong, X.; Wang, L.; Peng, X. Identification of Facet-Dependent Coordination Structures of Carboxylate Ligands on CdSe Nanocrystals. *J. Am. Chem. Soc.* **2019**, *141*, 15675–15683.
(52) Cooper, K. J.; Franco, M. A.; Gul, S.; Corrado, C.; Zhang, Z. C. Characterization of Primary Amine Capped CdSe, ZnSe, and ZnS Quantum Dots by FT-IR: Determination of Surface Bonding Interaction and Identification of Selective Desorption. *Langmuir* **2011**, *27*, 8486–8493
(53) Hens, Z.; Matins, C. J. A Solution NMR Toolbox for Characterizing the Surface Chemistry of Colloidal Nanocrystals. *Chem. Mater.* **2013**, *25*, 1211–1221.
(54) White, M. A.; Baumler, K. J.; Chen, Y.; Venkatesh, A.; Medina-Gonzalez, A. M.; Rossini, A. J.; Zaikina, J. V.; Chan, E. M.; Vela, J. Expanding the I-II-V Phase Space: Soft Synthesis of Polytypic Ternary and Binary Zinc Antimonides. *Chem. Mater.* **2018**, *30*, 6173–6182.
(55) White, M. A.; Miller, G. J.; Vela, J. Polytypism and Unique Site Preference in LiZnSb: A Superior Thermoelectric Reveals its True Colors. *J. Am. Chem. Soc.* **2016**, *138*, 14574–14577.
(56) White, M. A.; Thompson, M. J.; Miller, G. J.; Vela, J. Got LiZnP? Solution Phase Synthesis of Filled Tetrahedral Semiconductors in the Nanoregime. *Chem. Commun.* **2016**, *52*, 3497–3499.
(57) Tappan, B. A.; Horton, M. K.; Brutchey, R. L. Ligand-Mediated Phase Control in Colloidal $AgInSe_2$ Nanocrystals. *Chem. Mater.* **2020**, *32*, 2935–2945.
(58) Anderson, C. N.; Hendricks, P. M.; Choi, J. J.; Owen, S. J. Ligand Exchange and the Stoichiometry of Metal Chalcogenide Nanocrystals: Spectroscopic Observation of Facile Metal-Carboxylate Displacement and Binding. *J. Am. Chem. Soc.* **2013**, *135*, 18536–18548.
(59) Kalyuzhny, G; Murray, R. W. Ligand Effects on Optical Properties of CdSe Nanocrystals. *J. Phys. Chem. B* **2005**, *109*, 7012–7021.

(60) Kirkwood, N.; Monchen, J. O. V.; Crisp, R. W.; Grimaldi, G.; Borgstein, H. A. C.; Fossé I. D; Stam. W. V. D.; Infante, I.; Houtepen, A. J. Finding and Fixing Traps in II-VI and III-V Colloidal Quantum Dots: The Importance of Z-Type Ligand Passivation. *J. Am. Chem. Soc.* **2018**, *140*, 15712–15723.
(61) Munro, A. M; Plante, I.; Ng, M. S.; Ginger, D. S. Quantitative Study of the Effects of Surface Ligand Concentration on CdSe Nanocrystals Photoluminescence. *J. Phys. Chem. C* **2007**, *111*, 6220–6227.
(62) Kroupa, D. M.; Vörös, M.; Brawand, N. P.; McNichols, B. W.; Miller, E. M.; Gu, J.; Nozik, A. J.; Sellinger, A.; Galli, G.; Beard, M. C. Tuning Colloidal Quantum Dot Band Edge Positions Through Solution-Phase Surface Chemistry Modification. *Nat. Comm.* **2017,** *8*, 15257.
(63) Roo, D. J.; Ibáñez, M.; Geiregat, P.; Nedelcu, G.; Walravens, W.; Maes, J.; Martins, C. J.; Driessche, V. I.; Kovalenko, V. M.; Hens, Z. Highly Dynamic Ligand Binding and Light Absorption Coefficient of Cesium Lead Bromide Perovskite Nanocrystals. *ACS Nano* **2016**, *10*, 2071–2081.
(64) Talapin, D. V.; Lee, J.-S.; Kovalenko, M. V.; Shevchenko E. V. Prospects of Colloidal Nanocrystals for Electronic and Optoelectronic Applications. *Chem. Rev.* **2010**, *110*, 389–458.
(65) Palui, G.; Avellini, T.; Zhan, N.; Pan, F.; Gray, D.; Alabugin, I.; Mattoussi, H. Photoinduced Phase Transfer of Luminescent Quantum Dots to Polar and Aqueous Media. *J. Am. Chem. Soc.* **2012**, *134*, 16370–16378.
(66) Han, Z.; Eisenberg, R. Fuel from Water: The Photochemical Generation of Hydrogen from Water. *Acc. Res.* **2014**, *47*, 2537–2544.
(67) Das, A.; Han, Z.; Haghighi, G. M.; Eisenberg, R. Photogeneration of Hydrogen from Water Using CdSe Nanocrystals Demonstrating the Importance of Surface Exchange. *Proc. Natl. Acad. Sci. U.S.A.* **2013**, *110*, 16716–16723.
(68) Lv, H.; Wang, C.; Li, G.; Burke, R.; Krauss, D. T.; Gao, Y.; Eisenbeg, R. Semiconductor Quantum Dot-Sensitized Rainbow Photocathode for Effective Photoelectrochemical Hydrogen Generation. *Proc. Natl. Acad. Sci. U.S.A.* **2017**, *114*, 11297–11302.
(69) Pearson, R. G. Hard and Soft Acids and Bases. *J. Am. Chem. Soc.* **1963**, *85*, 3533–3539.
(70) Liang, K.; Mitzi, D. B.; Prikas, M. T. Synthesis and Characterization of Organic-Inorganic Perovskite Thin Films Prepared Using a Versatile Two-Step Dipping Technique. *Chem. Mater.* **1998**, *10*, 403–411.
(71) Liu, M.; Voznyy, O.; Sabatini, R.; García de Arquer, F. P.; Munir, R.; Balawi, Ahmed H.; Lan, X.; Fan, F.; Walters, G.; Kirmani, Ahmad R.; Hoogland, S.; Laquai, F.; Amassian, A.; Sargent, Edward H. Hybrid Organic–Inorganic Inks Flatten the Energy Landscape in Colloidal Quantum Dot Solids. *Nat. Mater.* **2016,** *16*, 258.
(72) Abel, K. A.; Fitzgerald, P. A.; Wang, T-Y.; Regier, T. Z.; Raudsepp, M.; Ringer, S. P.; Warr, G. G.; Veggel, F. C. J. M. J. Probing the Structure of Colloidal Core/Shell Quantum Dots Formed by Cation Exchange. *J. Phys. Chem. C* **2012**, 116, 3968–3978.
(73) Lechner, R. T.; Fritz-Popovski, G.; Yarema, M.; Heiss, W.; Hoell, A.; Schülli, T. U.; Primetzhofer, D.; Eibelhuber, M.; Paris, O. Crystal Phase Transitions in the Shell of PbS/CdS Core/Shell Nanocrystals Influences Photoluminescence Intensity. *Chem. Mater.* **2014***, 26*, 5914–5922.
(74) Pietryga, J. M.; Werder, D. J.; Williams, D. J.; Casson, J. L.; Schaller, R. D.; Klimov, V. I.; Hollingsworth, J. L. Utilizing the Lability of Lead Selenide to Produce Heterostructured Nanocrystals with Bright, Stable Infrared Emission. *J. Am. Chem. Soc.* **2008**, *130*, 4879–4885.
(75) Sagar, L, K.; Walravens, W.; Zhao, Q.; Vantomme, A.; Geiregat, P.; Hens, Z. PbS/CdS Core/Shell Quantum Dots by Additive, Layer-by-Layer Shell Growth. *Chem. Mater.* **2016**, *28*, 6953–6959.
(76) Yuan, M.; Liu, M.; Sargent, E. H. Colloidal Quantum Dot Solids for Solution-Processed Solar Cells. *Nat. Energy* **2016,** *1*, 16016.
(77) Sanehira, E. M.; Marshall, A. R.; Christians, J. A.; Harvey, S. P.; Ciesielski, P. N.; Wheeler, L. M.; Schulz, P.; Lin, L. Y.; Beard, M. C.; Luther, J. M. Enhanced Mobility $CsPbI_3$ Quantum Dot Arrays for Record-Efficiency, High-Voltage Photovoltaic Cells. *Sci. Adv.* **2017**, *3*, eaao4204.
(78) Lu, K.; Wang, Y.; Liu, Z.; Han, L.; Shi, G.; Fang, H.; Chen, J.; Ye, X.; Chen, S.; Yang, F.; Shulga, A. G.; Wu, T.; Gu, M.; Zhou, S.; Fan, J.; Loi, M. A.; Ma, W. High-Efficiency PbS Quantum-Dot Solar Cells with Greatly Simplified Fabrication Processing via "Solveng-Curing". *Adv. Mater.* **2018**, 30, 1707572.
(79) Sayevich, V.; Gaponik, N.; Plötner, M.; Kruszynska, M.; Gemming, T.; Dzhagan, V. M.; Akhavan, S.; Zahn, D. R. T.; Demir, H. V.; Eychmüller, A. Stable Dispersion of Iodide-Capped PbSe Quantum Dots for High-Performance Low-Temperature Processed Electronics and Optoelectronics. *Chem. Mater.* **2015**, *27*, 4328–4337
(80) Abargues, R.; Navarro, J.; Rodríguez-Cantó, P. J.; Maulu, A.; Sánchez-Royo, J. F.; Martínez-Pastor, J. P. Enhancing the Photocatalytic Properties of PbS QD Solids: The Ligand Exchange Approach. *Nanoscale* **2019**, *11*, 1978–1987.
(81) Chwang, R.; Smith, B. J.; Crowell, C. R. Contact Size Effects on the Van Der Pauw Method for Resistivity and Hall Coefficient Measurement. *Solid-State Elctron.* **1974**, *17*, 1217–1227.
(82) Shaw, S.; Yuan, B.; Tian, X.; Miller, K. J..; Cote, B. M.; Colaux, J. L.; Migliori, A.; Panthani, M. G.; Cademartiri, L. Building Materials from Colloidal Nanocrystal Arrays: Preventing Crack Formation During Ligand Removal by Controlling Structure and Solvation. *Adv. Mater.* **2016**, *28*, 8892–8899.
(83) Crisp, R. W.; Kroupa, D. M.; Marshall A. R.; Miller, E. M; Zhang, J.; Beard, M. C.; Luther, J. M.; Metal Halide Solid-State Surface Treatment for High Efficiency PbS and PbSe QD Solar Cells. *Sci. Rep.* **2015**, *5*, 9945.

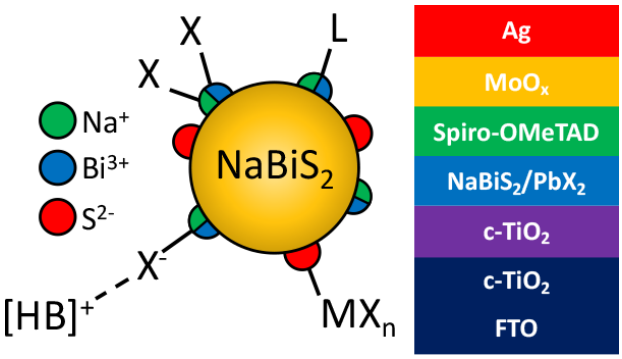
X
L
X
Na+
Bi3+
S2-
NaBiS2
X-
[HB]+
MXn
Ag
MoOx
Spiro-OMeTAD
NaBiS2/PbX2
c-TiO2
c-TiO2
FTO

TOC Graphic